Article

Synthesis of Hureaulite Mn$_5$(H$_2$O)$_4$(PO$_3$OH)$_2$(PO$_4$)$_2$ with an Open 3D Network Structure as Electrode Material for Electrochemical Capacitors

Cesar Iván García Guajardo [1], Jorge Alexis Zúñiga Martínez [1,2,3], Roxana Berlanga Pérez [1,3], Luis Alberto López Pavón [2,3] and Raúl Lucio Porto [1,2,3,*]

[1] Centro de Innovación, Investigación y Desarrollo en Ingeniería y Tecnología, Universidad Autónoma de Nuevo León, Apodaca 66600, Nuevo León, Mexico; jorge.zunigamr@uanl.edu.mx (J.A.Z.M.); roxana.berlangapz@uanl.edu.mx (R.B.P.)

[2] Centro de Innovación e Ingeniería en Tecnología Inteligente, Universidad Autónoma de Nuevo León, San Nicolás de los Garza 66455, Nuevo León, Mexico

[3] Facultad de Ingeniería Mecánica y Eléctrica, Universidad Autónoma de Nuevo León, San Nicolás de los Garza 66455, Nuevo León, Mexico

* Correspondence: raul.lucioprt@uanl.edu.mx; Tex.: +52-(81)-1340-4000 (ext. 1504)

Abstract: Mn$_5$(H$_2$O)$_4$(PO$_3$OH)$_2$(PO$_4$)$_2$ with an open 3D network was prepared and studied as electrode material for electrochemical capacitors. The material exhibits a tunnel structure along the c axis, characterized by a hydrogen bond network formed by water molecules bonded to MnO$_6$ octahedra and PO$_3$-OH tetrahedra units, the latter containing an acidic proton. Electrochemical studies were conducted on both alkaline and neutral electrolytes, revealing a profile indicative of a rapid faradaic process coupled with pseudocapacitance and electrochemical double-layer capacitance. This study proposes a mechanism that involves the interaction between the acidic proton in the tunnel structure and OH$^-$ ions from the electrolyte, which diffuse through the hydrogen bond network. The material achieved a maximum specific capacitance of 184 Fg^{-1} at a scan rate of 5 mVs^{-1}, with an areal capacitance of 4600 μFcm^{-2} in 3M KOH. This demonstrates its potential as a high-performance electrode for energy storage applications.

Keywords: manganese phosphate; fast electrochemical energy storage; ion intercalation

1. Introduction

Electrochemical energy storage devices are the principal source of portable energy for modern electronic technologies and electric vehicles. Batteries are the most common devices used due to their high energy density. However, they require long charging time, and they suffer from low power densities and short life cycles [1–3]. Recently, electrochemical capacitors (ECs) have emerged as a new energy storage device that outperform batteries in terms of power density and life cycle, and as micro-devices, they can also store more energy [4–7]. This is possible due to their charge storage mechanisms. Electrical double-layer (EDL) capacitors store charge through electrostatic interactions between the electrode surface and the electrolyte ions, practically with a lack of faradaic reactions. A second mechanism known as pseudocapacitance, involves fast and reversible successive surface redox reactions, allowing for more charge storage than electrical double-layer capacitors and in less time than batteries [1,2,8]. In both mechanisms, a fundamental principle of electrochemical capacitors must be fulfilled, a linear dependence of charge within the applied voltage, leading to a constant known as capacitance [8].

Nevertheless, the ion intercalation/deintercalation process has been reported for ECs in layered metal oxides such as δ-MnO$_2$, V$_2$O$_5$, and WO$_3 \bullet$2H$_2$O [9–12] and more recently for transition metal phosphates like MnPO$_4 \bullet$H$_2$O, VOPO$_4 \bullet$2H$_2$O, K$_{0.5}$VOPO$_4 \bullet$1.5H$_2$O, and Mn$_3$(PO$_4$)$_2 \cdot$3H$_2$O [13–16]. This process occurs in the 1D, 2D, or 3D tunnels of the crystalline

structure of the electrode materials. According to the above reports, the presence of water molecules in the tunnels is essential for the ion intercalation/deintercalation process. Although this process is typically found in battery-type electrode materials [12,14,15], the electrochemical signature of these materials indicates a capacitive behavior, sometimes coupled with a Faradaic process. For transition metal phosphates, the charge can be completed in 6 to 10 s. Additionally, the areal capacitance ranges are from 500 to 118 μFcm^{-2} for layered vanadium phosphates and 1350 μFcm^{-2} for $MnPO_4 \bullet H_2O$ [13–15]. These charge and discharge rates and capacitances are among the highest values reported for transition metal-based electrodes [5,11]. According to previous reports [14,15], the ion intercalation/deintercalation process coupled with electric double-layer capacitance and pseudocapacitance is essential for increasing the stored charge while maintaining both the capacitive behavior and the high charge and discharge rates.

Recently, $Mn_5(H_2O)_4(PO_3OH)_2(PO_4)_2$ has been proposed as electrode material for Li-ion batteries [17]. In this contribution, a simple precipitation route is reported to obtain $Mn_5(H_2O)_4(PO_3OH)_2(PO_4)_2$, which has an open 3D network structure. Its electrochemical behavior as an electrode material for ECs is shown for the first time in several electrolytes. The deconvoluted cyclic voltammograms indicate the presence of the three charge storage mechanisms: EDL capacitance, pseudocapacitance, and ion intercalation/deintercalation process through the Grotthuss proton conduction mechanism. The effect of the crystalline structure on the charge stored mechanism is also highlighted. The performance of this electrode material was also evaluated by chronopotentiometry (charge and discharge at constant current) using a two-electrode cell (Swagelok cell).

2. Methodology

2.1. Synthesis of $Mn_5(H_2O)_4(PO_3OH)_2(PO_4)_2$

A solution of sodium dodecyl sulfate (SDS, Sigma-Aldrich, St. Louis, MI, USA, 99%) was prepared with a concentration of 5%w. Then, $MnCl_2 \bullet 4H_2O$ (Sigma-Aldrich, St. Louis, MI, USA, 97%) was added until a molar ratio SDS/Mn of 1.8 was fixed. The temperature of the solution was increased to 70 °C and kept for one hour. Then, a solution of K_2HPO_4 (Sigma-Aldrich, St. Louis, MI, USA, 98%) was added dropwise to keep a molar ratio Mn/K_2HPO_4 of 1. The above mixture was kept at 70 °C for 24 h. Then, a white powder was recovered by filtration, washed several times with water and acetone, and dried at room temperature.

2.2. Material Characterization

X-ray diffraction patterns (XRDs) were collected in an Empyrean Panalytical diffractometer (Malvern Panalytical, Malvern, UK) operated at 45 kV and 40 mA with a CuK_α radiation (λ = 1.5406 Å). The scans were performed with a step scan of 0.02° and 1 s per step in a continuous mode in the 2θ range from 5 to 90°. An FEI Nova NanoSEM scanning electron microscope (FEI company, Hillsboro, OH, USA) with a Field Emission Gun was used to analyze the morphology of the nanomaterial. The BET surface area was obtained from an Autosorb II (Anton Paar, Graz, Austria). RAMAN analysis was performed on a Thermo Scientific DXR Microscope 3xi spectrophotometer (Thermo scientific, Waltham, MA, USA) with a 512 nm Argon laser source in the range of 100 to 3500 cm^{-1} with 32 scans. A Thermo Scientific spectrophotometer model Nicolet 6700 (Thermo scientific, Waltham, MA, USA) was used to perform FTIR analysis. A ratio of 1:50 (sample–KBr) was used to prepare the pellet. A resolution of 4 cm^{-1} and 32 scans were used to collect the spectrum.

2.3. Electrochemical Characterization

The preparation of the electrodes consisted in a mixture of active material, carbon black (Orion SA, Senningerberg, Luxemburg), and PTFE (Sigma-Aldrich, St. Louis, MI, USA) in a 70:20:10 weight ratio, respectively. Ethanol (CTR scientific, Monterrey, NL, Mexico) was added to the above mixture to obtain a paste that was rolled into 100 μm thick films and pressed in a stainless-steel grid at 1 GPa. The mas loading of active material was 7 $mgcm^{-2}$.

A three-electrode cell was assembled with a platinum grid as a counter-electrode and as a reference electrode Ag/AgCl for neutral electrolytes and Hg/HgO for alkaline electrolytes. The neutral electrolytes were 1M Na_2SO_4 and 5M $LiNO_3$. The alkaline electrolytes were 1M KOH, 3M KOH, 3M NaOH, 3M LiOH, 3M K_3PO_4, and 3M tetramethylammonium hydroxide (TMAOH). All the electrolytes were provided by Sigma-Aldrich (Sigma-Aldrich, St. Louis, MI, USA). The two-electrode cell, a Swagelok-type cell, was assembled in a symmetric configuration with fiberglass (Sigma-Aldrich) as a separator wetted with 0.5 mL of 5M KOH electrolyte. The electrochemical behavior of the electrode material was studied in a VMP-3 potentiostat-galvanostat (Biologic Instruments, Seyssinet-Pariset, France) by performing cyclic voltammetry, chronopotentiometry, and electrochemical impedance spectroscopy (EIS).

The specific capacitance C (Fg^{-1}) was estimated from the average charge obtained by integrating the area of the cyclic voltammogram during oxidation and reduction, as is shown in Equation (1), where Q is the charge in C, ΔV is the electrochemical window in volts, and m is the mass of active material in grams:

$$C\left(Fg^{-1}\right) = \frac{Q}{\Delta V m} \tag{1}$$

The specific energy and power densities of the two-electrode cell (Swagelok, S4R, Castelnau-le-Lez, France) were estimated with Equations (2) and (3), respectively, from chronopotentiometry experiments (constant current charge–discharge). Here, E is the specific energy in $Whkg^{-1}$, I is the current in A, t is the discharge time in s, V is the applied voltage in volts, and m is the mass of active material in kg. P is the specific power in Wkg^{-1}, and t is the discharge time in s.

$$E = \frac{1}{2} \frac{ItV}{m} \tag{2}$$

$$P = \frac{E}{t} \tag{3}$$

For the EIS tests, an amplitude of 10 mV was used with a frequency range from 10 mHz to 100 kHz. The spectra were acquired at the open-circuit potential.

3. Results

The novel synthetic route leads to a manganese phosphate with a single crystalline phase that can be indexed to $Mn_5(H_2O)_4(PO_3OH)_2(PO_4)_2$ (hureaulite), confirmed by the XRD (JCPDS card 01-076-0804) shown in Figure 1a. The crystal lattice is monoclinic with a space group C2/c. The crystalline structure consists of an open 3D network built up with pentamers that consist of corner-sharing Mn^{2+} octahedral (MnO_6) units leading to a composition of Mn_5O_{22} (see Figure 1b). The pentamers are also linked together by corner-sharing with six oxygen atoms along the *b*-axis and share vertices with PO_4 and PO_3-OH tetrahedra, ending with a composition of Mn_5O_{18} (see Figure 1c). The four water molecules are bonded to Mn^{2+} ions as ligand groups [18,19]. Along the c axis, 1D channels are formed with a size of around 6.10 X 3.0 Å. More interesting is that the group O-H in $PO_3(OH)$ tetrahedra and H_2O molecules coordinated to Mn^{2+} in octahedral units point into the open structure of this channel (see Figure 1d). The free O-H group in $PO_3(OH)$ tetrahedra is acid in nature [20], and Moore and Araki were the first to recognize that, by neutralizing the acid group, cations (Li^+, Na^+, Ca^{2+}) could be intercalated into the 1D tunnels [18]. The water molecules bound to Mn^{2+} atoms form hydrogen bonds with the nearest oxygen atoms of the octahedral units (MnO_6), and the $PO_3(OH)$ and PO_4 groups, leading to a network of hydrogen bonds along the channel, here in the pocket (see Figure 1d) [18–22]. Recently, Hartl et al. reported the proton conductivity of hureaulite along this hydrogen bonding network [22]. Additionally, more channels arise across the crystalline structure with a smaller size than the above-mentioned. Thus, an open 3D framework arises (see Figure 1e–g).
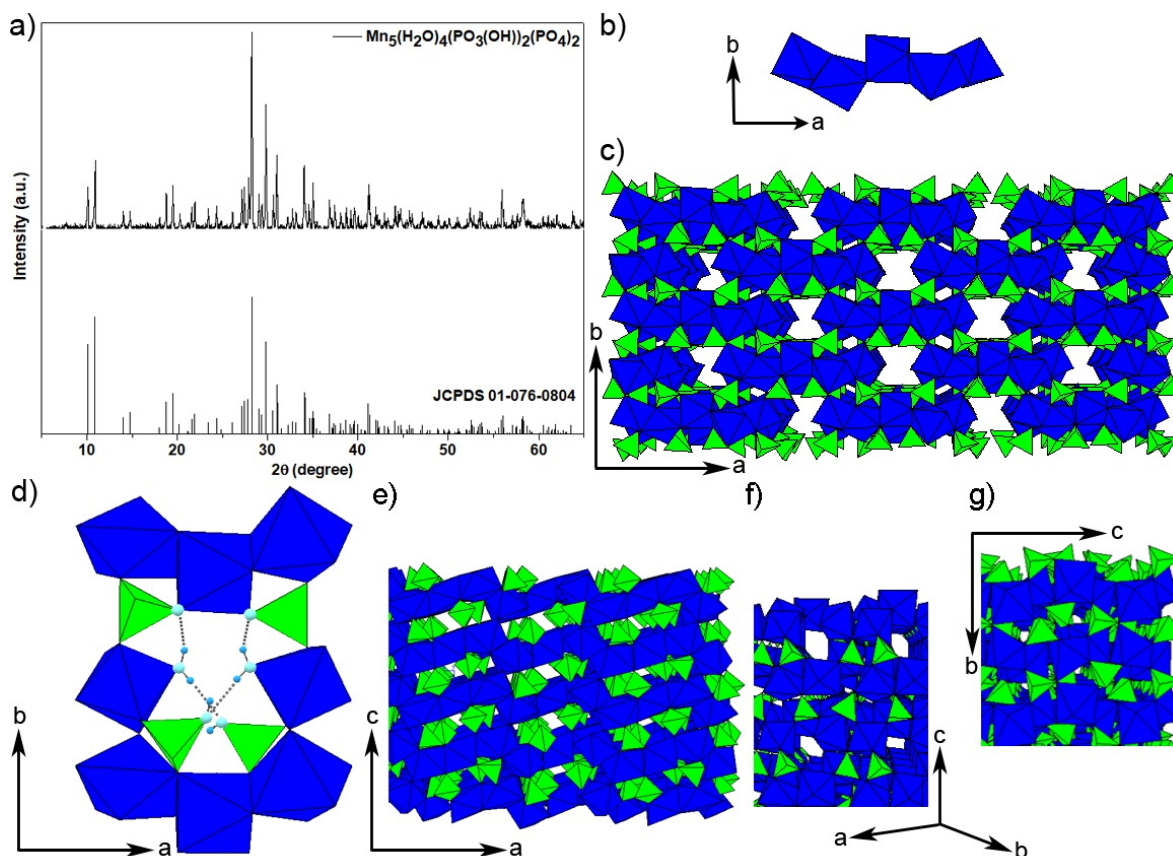
Figure 1. (**a**) XRD of $Mn_5(H_2O)_4(PO_3OH)_2(PO_4)_2$. (**b**) Mn_5O_{22} units. (**c**) Crystalline structure of $Mn_5(H_2O)_4(PO_3OH)_2(PO_4)_2$. (**d**) Open structure of the channel (pocket) showing hydrogen bonding with water molecules and PO_3-OH groups. (**e**–**g**) Tunnels in the crystalline structure of $Mn_5(H_2O)_4(PO_3OH)_2(PO_4)_2$ across different axes.

Figure 2a shows the SEM image that reveals the morphology of the prepared hureaulite. Interconnected plates with a "star" configuration are observed (see Figure 2a, inset). The plates are nanostructured with a thickness of around 40 nm, a length in the order of 3 μm, and a cross-section around 700 nm. To our knowledge, this is the first time that hureaulite particles with a nanostructured plate morphology have been prepared. The typical obtained morphology for this material by precipitation or solvothermal methods is rodlike nanoparticles and prismatic crystals with a size from a few micrometers up to a few millimeters [20,22–24]. Plate-like particles are also reported with a length of around 14 μm and a thickness of around 2.5 μm [25]. In our approach, the use of SDS as a structuring directing agent allows for the preparation of nanostructured hureaulite particles. However, the specific surface area is as low as 4 m^2g^{-1}, and the BET isotherm indicates the absence of mesopores (see Figure S1).

The RAMAN spectrum shown in Figure 2b confirms the formation of hureaulite, $Mn_5(H_2O)_4(PO_3OH)_2(PO_4)_2$, according to the spectroscopic study realized by Frost et al. [26]. Several vibrational bands are found in the region of 3000 to 3500 cm^{-1}, indicating that water molecules are not equivalent in the crystalline structure. The stretching vibrations of O-H in H_2O molecules are ascribed to the 3479 cm^{-1}, 3345 cm^{-1}, 3229 cm^{-1}, 3127 cm^{-1}, and 3042 cm^{-1} bands. The antisymmetric stretching vibrations of the HPO_4^{2-} and PO_4^{3-} bands are found at 1107cm^{-1}, 1078cm^{-1}, 1042 cm^{-1}, 1019 cm^{-1}, and 1000cm^{-1}. The symmetric stretching vibration of the PO_4^{3-} group is observed at 988 cm^{-1} and 968 cm^{-1}. The intense band at 945 cm^{-1} is assigned to the stretching vibrations of the P-O bonds in the PO_3-OH group. The single peak observed at 726 cm^{-1} is attributed to the H_2O liberational mode. Nearby are four weak bands at 531 cm^{-1}, 559 cm^{-1}, 582 cm^{-1}, and 591 cm^{-1},

assigned to the out-of-plane bending modes of HPO_4 and PO_4. The bending modes of PO_3-OH and PO_4 are found at 410 cm^{-1} and 452 cm^{-1}. Finally, the Mn-O bending band is observed at 379 cm^{-1}.
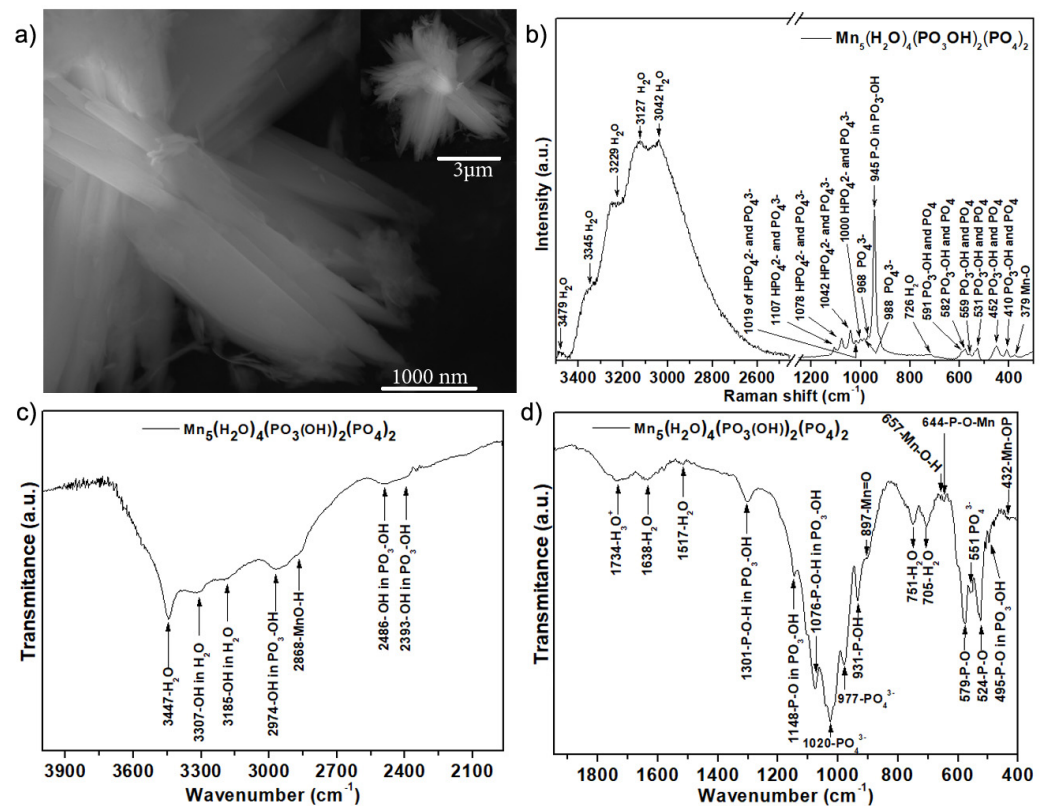

Figure 2. (**a**) SEM image of $Mn_5(H_2O)_4(PO_3OH)_2(PO_4)_2$. (**b**) RAMAN spectrum. (**c,d**) FTIR spectrum of $Mn_5(H_2O)_4(PO_3OH)_2(PO_4)_2$.

In Figure 2c,d, the FTIR spectrum of hureaulite is depicted. Several bands of the O-H group are observed indicating that its vibrations correspond to a non-equivalent site in the crystalline structure. The band at 3447 cm^{-1} belongs to the asymmetric O-H stretching in H_2O molecules. The symmetric stretching mode of O-H in H_2O molecules is observed as a doublet at 3307 and 3185 cm^{-1} [25]. The band located at 2974 cm^{-1} is the asymmetric stretching of O-H in the PO_3-OH group [25]. The band at 2868 cm^{-1} corresponds to the MnO-H group [27,28]. The bands at 2486 and 2393 cm^{-1} correspond to the symmetric stretching of O-H in PO_3-OH. The bands at 1734 and 1638 cm^{-1} are associated with strong hydrogen bonds of H_2O water molecules [26] and correspond to the vibration of H_3O^+ species [23,27] and in-plane bending vibration of H-O-H [26,27], respectively. The band located at 1517 cm^{-1} also indicates the bending vibration of H-O-H molecules [25]. Hence, this agrees with the hydrogen bonding network of hureaulite determined via XRD data by several authors. It has been recognized that the band at 1301 cm^{-1} belongs to the P-O-H in-plane vibration in the PO_3-OH group, and corresponds only to the crystalline structure of hureaulite; other manganese phosphates with the PO_3-OH group show a band at lower wavenumbers [24]. The bands at 1148 and 1076 cm^{-1} correspond to the antisymmetric stretching vibration of the P-O group in PO_3-OH [25,26,29]. The bands at 1020 and 977 cm^{-1} are assigned to the symmetric stretching vibrations of PO_4^{3-} group [26]. The symmetric stretching vibration of the P-OH group is found at 931 cm^{-1} [25,26]. The shoulder at 897 cm^{-1} corresponds to the Mn=O group [23]. Both bands, at 751 and 705 cm^{-1}, correspond to the wagging and twisting of H_2O molecules. The bending vibration of the Mn-O-H and the P-O-Mn groups are assigned to bands located at 657 and 644 cm^{-1}, respectively [27]. The bands at 579 and 524 cm^{-1} belong to the in-plane bending vibration of the P-O group [23]. The band at 551 cm^{-1} corresponds to PO_4^{3-} [28]. The band

at 495 cm^{-1} belongs to the P-O in PO$_3$-OH [25]. Finally, the band at 432 cm^{-1} is assigned to the Mn-OP group [28]. Thus, the FTIR spectrum confirms that the hureaulite is built up with PO$_3$-OH and PO$_4$ groups and that the H$_2$O molecules are bonded to Mn^{2+}, which evidence the hydrogen bonding, in agreement with the reports of the crystalline structure determined by XRD analyses.

The electrochemical behavior is studied by cyclic voltammetry. In Figure 3a,b,e, the cyclic voltammograms in alkaline and neutral media are shown at the scan rate of 5 mVs^{-1}. The electrochemical signature of the voltammograms in all tested electrolytes shows reversible waves, which suggests a faradaic process superimposed to pseudocapacitive and capacitive behavior of the hureaulite. In 3M KOH, the maximum intensity of the waves occurs at −0.23 and −0.01 V vs. Hg/HgO in the anodic scan and at −0.19 and −0.08 V vs. Hg/HgO in the cathodic scan. On the contrary, only a couple of redox peaks are visible in 1M KOH, located at −0.03 V vs. Hg/HgO in the anodic scan and at −0.12 V vs. Hg/HgO in the cathodic scan. In the case of 3M NaOH, the cyclic voltammogram depicts a redox wave at 0.12 V vs. Hg/HgO in the anodic current and at 0.04 V vs. Hg/HgO in the cathodic current. For 3M LiOH, only a couple of waves are observed at −0.02 V vs. Hg/HgO in the anodic scan and −0.11 V vs. Hg/HgO in the cathodic scan. Interestingly, a couple of well-defined reversible peaks are observed in 3M K$_3$PO$_4$ (see Figure 3b) at −0.43 V vs. Hg/HgO in the anodic scan and −0.45 in the cathodic scan coupled with two waves at −0.69 V vs. Hg/HgO in the anodic scan and −0.72 in the cathodic scan. In 3M TMAOH, the voltammogram also depicts a redox wave at −0.33 V (anodic scan) vs. Hg/HgO and −0.42 (cathodic scan) V vs. Hg/HgO. Furthermore, in 3M KOH, 1M KOH, 3M NaOH, 3M LiOH, and 3M TMAOH, the electrochemical window is up to 0.7 V and 0.8 V in 3M K$_3$PO$_4$. The electrochemical behavior remains up to 100 mVs^{-1} for the 3M KOH and 3M LiOH (see Figure S2a,b). The fast response to high scan rates is typical of transition metal phosphates [13–16,30–32]. However, in the case of 1M KOH and 3M NaOH, the electrochemical behavior remains up to 25 mVs^{-1} (see Figure S2c,d). In 3M TMAOH, the electrochemical behavior remains up to 2000 mVs^{-1} (see Figure S3a,b). In 3M K$_3$PO$_4$, the electrochemical behavior remains up to 5000 mVs^{-1} (see Figure S3c,d) with redox waves in the voltammograms. This is the faster response to a high scan rate that involves a faradaic process that has been reported in alkaline electrolytes for transition metal-based electrodes [5,13,14,16]. Nevertheless, the highest specific capacitance for hureaulite is 184 Fg^{-1} in 3M KOH, 165 Fg^{-1} in 1M KOH, 111 Fg^{-1} in 3M NaOH, and only 58 Fg^{-1} in 3M LiOH (see Figure 3c) at 5 mVs^{-1}. It is worth highlighting that even at the high scan rate of 100 mVs^{-1}, the specific capacitance is 100 Fg^{-1} in 3M KOH (a loss of around 46 percent of the capacitance), and in 3M LiOH, at the same scan rate, the specific capacitance is 26 Fg^{-1} (a loss around 55 percent of the capacitance). A larger amount of loss stored charge as a function of the scan rate is observed in the cases of manganese oxides [33], metal phosphates [32], metal nitrides [34], and carbon-based electrodes [35]. The specific capacitance in 3M K$_3$PO$_4$ is only 8 Fg^{-1} and 22 Fg^{-1} in 3M TMAOH at 5 mVs^{-1} lower values than in the previous alkaline electrolytes. In order to clarify the effect of pH and electrolyte composition and concentration on the electrochemical behavior, the specific capacitance at 5 mVs^{-1} is shown versus the electrolyte pH in Figure 3d. In alkali hydroxides, the trend is clear: the specific capacitance increases with the electrolyte pH, regardless of any type of cation. However, the pH of 1M KOH and 3M NaOH is 13.8 and 14.0, respectively, but the specific capacitance is larger for the former electrolyte (despite the higher concentration of NaOH), indicating that K$^+$ ions have a positive effect over Na$^+$ and Li$^+$ ions on the charge storage process. Interestingly, 3M K$_3$PO$_4$ and 3M KOH electrolytes show very close pH values, 14.0 and 14.6, respectively, and the former has the lowest specific capacitance in alkaline electrolytes. Thus, the 3M K$_3$PO$_4$ and 3M KOH drastically differ in the specific capacitance but with similar pH values, indicating that OH$^-$ ions play a key role in the charge storage processes. However, from the comparison between 3M TMAOH and 3M KOH, it is evident that the TMA$^+$ cations are detrimental to the charge storage processes. The above results suggest that the active ions for the charge storage process are OH$^-$ and

K^+. Additionally, the significative difference in specific capacitance at all scan rates, in the presence of these electrolytes, must be addressed to the size of their ions. The larger bare or hydrated ion sizes of PO_4^{3-} (2.23 and 3.39 Å, respectively) compared to the sizes of OH^- (1.76 and 3.00 Å, respectively) [36] could explain the difference in specific capacitance. The smaller sizes of OH^- enhance its diffusion through the pocket (an intercalation process) reacting with the acid groups and forming hydrogen bonds. However, the lower specific capacitance observed in 3M LiOH and 3M NaOH compared to 3M KOH seems to be related to the hydrated ion sizes of cations that are 3.82, 3.58, and 3.31 Å, respectively [36]. Thus, the larger the hydrated ion size, the lower the specific capacitance. In the case of 3M TMAOH, the low specific capacitance is also explained by the large, hydrated ion size of the $N^+(CH_3)_4$ ion (3.67 Å), compared to the K^+ ion. Thus, the larger size of the quaternary ammonium ion hinders the charge storage process.
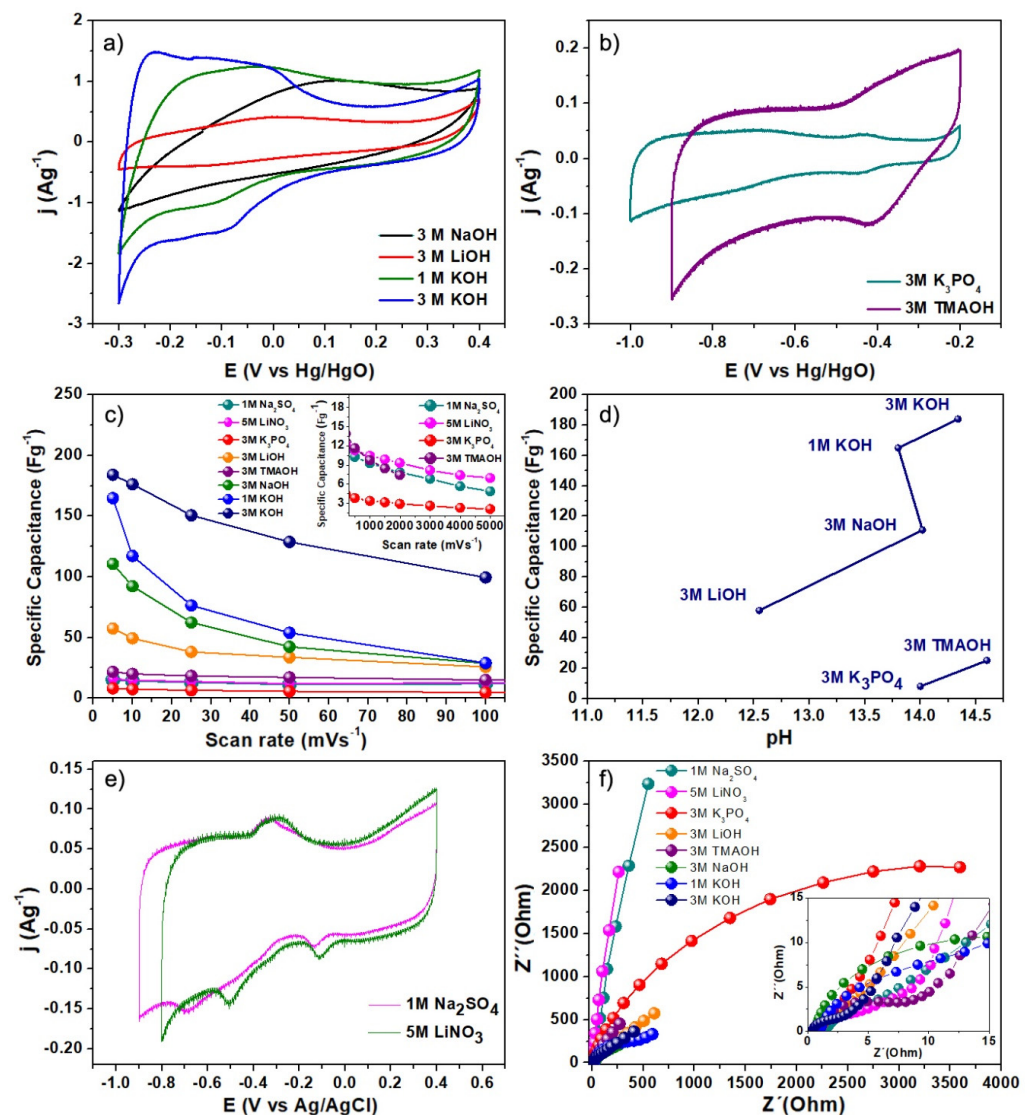

Figure 3. Cyclic voltammograms of $Mn_5(H_2O)_4(PO_3OH)_2(PO_4)_2$ at 5 mVs^{-1} in (**a**) 3M KOH, 1M KOH, 3M NaOH, and 3M LiOH. (**b**) Cyclic voltammogram of $Mn_5(H_2O)_4(PO_3OH)_2(PO_4)_2$ at 5 mVs^{-1} in 3M K_3PO_4 and 3M TMAOH. (**c**) Specific capacitance of $Mn_5(H_2O)_4(PO_3OH)_2(PO_4)_2$ in different electrolytes as a function of the scan rate. (**d**) Specific capacitance of $Mn_5(H_2O)_4(PO_3OH)_2(PO_4)_2$ at 5 mVs^{-1} in different electrolytes as a function of pH. (**e**) Cyclic voltammogram of $Mn_5(H_2O)_4(PO_3OH)_2(PO_4)_2$ at 5 mVs^{-1} in 5M $LiNO_3$ and 1M Na_2SO_4. (**f**) EIS spectra of $Mn_5(H_2O)_4(PO_3OH)_2(PO_4)_2$ in different electrolytes.

In neutral electrolytes, wider electrochemical windows are observed than in alkaline electrolytes (see Figure 3e), 1.2 V for 5M $LiNO_3$ and 1.3 V for 1M Na_2SO_4 vs. Ag/AgCl. Redox peaks are observed in 5M $LiNO_3$ at −0.3 V vs. Ag/AgCl in the anodic scan and −0.5 and −0.11 V vs. Ag/AgCl in the cathodic scan. For 1M Na_2SO_4, the peaks are centered at −0.33 V vs. Ag/AgCl in the anodic scan and −0.69 and 0.13 V vs. Ag/AgCl in the cathodic scan. An impressive response for both neutral electrolytes is observed up to 5000 mVs^{-1} (see Figure S4a–d). Even at such high scan rates, redox waves are evidenced, suggesting a fast faradaic process. These are the faster responses to a high scan rate, which involves a faradaic process that has been reported in neutral electrolytes for transition metal-based electrodes [5,33,34,37,38]. The specific capacitances in 5M $LiNO_3$ and 1M Na_2SO_4 electrolytes are 16 Fg^{-1} and 15 Fg^{-1}, respectively (see Figure 3c), which are lower values than in alkaline electrolytes. The reversible redox waves can be attributed to the faradaic process limited to the surface. Thus, the low specific surface (4 m^2g^{-1}) of the prepared hureaulite explains the low-specific-surface charge storage. Additionally, the neutral pH of the electrolytes prevents their reaction with the acid hydrogens of the PO_3-OH groups hindering the intercalation process. The NO_3^- and SO_4^- ions are weaker bases than OH^-, distinguished by their large bare and hydrated ion sizes, measuring 2.64 and 3.35 Å for NO_3^-, and 2.90 and 3.79 Å for SO_4^- [36], respectively, surpassing those of OH^- ions. This leads to a decreased proton intercalation and a reduced stored charge. Therefore, the high basicity of the electrolytes enhances the reactivity with protons located in the pocket.

Recent studies have recognized that the charge storage process through ion intercalation in $MnPO_4 \bullet H_2O$, $VOPO_4$, and $NbOPO_4$ is influenced by the ion size (whether bare or hydrated), as well as the crystalline and local structures, including the chemical composition of the channels [13,39]. This finding has been further substantiated for $VOPO_4 \bullet 2H_2O$ and $K_{0.5}VOPO_4 \bullet 1.5H_2O$ [14,15].

In Figure 3f, the impedance spectra acquired at the open circuit potential of $Mn_5(H_2O)_4(PO_3OH)_2(PO_4)_2$ are shown. The equivalent series resistance (ESR) values in different electrolytes decrease in the following order: 3M KOH > 3M LiOH > 3M NaOH > 5M $LiNO_3$ > 3M TMAOH > 1M KOH = 3M K_3PO_4 > 1M Na_2SO_4 (insert in Figure 3f). Therefore, as the electrodes are manufactured in the same way, these resistances originated from the different active ion sizes and concentrations of the electrolytes. In the high-frequency region of the spectra (insert in Figure 3f), the diameter of the semi-circle is associated with the charge transfer resistance. The semi-circle diameter increases in the following order: 3M KOH < 3M LiOH < 3M TMAOH < 1M KOH < 3M NaOH < 3M K_3PO_4. The electrolyte K_3PO_4 shows the largest charge transfer resistance (semi-circle) among all the tested electrolytes, suggesting a hindered charge storage process by the ion size of the PO_4^{3-} group and its lower reactivity with the hydrogens of the PO_3-OH groups located in the pocket. In neutral electrolytes, the diameters of the semi-circles (1M Na_2SO_4, 5M $LiNO_3$) are very similar and larger than in alkaline electrolytes. This originated from the larger anion sizes of neutral electrolytes compared to the OH^- ion and their weaker basicity.

In the middle- and low-frequency regions of the spectra, the behavior drastically differs from one electrolyte to another. For alkaline electrolytes, a straight line around 45 degrees indicates a Warbug impedance, a charge storage process limited by diffusion, such as ion intercalation [14]. Just in the case of the K_3PO_4, a large semi-circle is observed in the low-frequency region. This probably originated from a large charge transfer resistance. In the neutral electrolytes, a bent line parallel to the Z'' axis indicates a dominant capacitive (electric double-layer and pseudocapacitive) charge storage process, which is in agreement with previous results of cyclic voltammetry.

It is well known that the specific capacitance increases with the surface area [38]. Thus, the areal capacitance allows a comparison of the performance between electrode materials with different specific surface areas. Table 1 shows the areal capacitances of some families of electrode materials and some transition metal phosphates to compare with the $Mn_5(H_2O)_4(PO_3OH)_2(PO_4)_2$ synthesized in this work. The new electrode material shows

the highest areal capacitance reported in the literature on alkaline electrolytes. Hence, the open 3D network, especially the pocket, is the main reason for the higher areal capacitance.

Table 1. Areal capacitances of electrode materials for electrochemical capacitors.

Electrode	Areal Capacitance (μFcm^{-2})	Ref
Double-Layer Capacitance	50	[40,41]
Ruthenium Oxides	390	[42]
Metal Nitrides	50–300	[38]
Manganese Oxides	110–123	[43]
$MnPO_4$ 3M KOH	1350	[13]
$VOPO_4 \bullet 2H_2O$ in 3M LiOH	500	[14]
$VOPO_4 \bullet 2H_2O$ in 3M KOH	430	[14]
$VOPO_4 \bullet 2H_2O$ in 3M $LiNO_3$	240	[14]
$Mn_5(H_2O)_4(PO_3OH)_2(PO_4)_2$ in 3M KOH	4600	This Work
$Mn_5(H_2O)_4(PO_3OH)_2(PO_4)_2$ in 1M KOH	4100	This Work
$Mn_5(H_2O)_4(PO_3OH)_2(PO_4)_2$ in 3M NaOH	2870	This Work
$Mn_5(H_2O)_4(PO_3OH)_2(PO_4)_2$ in 3M LiOH	1450	This Work
$Mn_5(H_2O)_4(PO_3OH)_2(PO_4)_2$ in 3M TMAOH	550	This Work
$Mn_5(H_2O)_4(PO_3OH)_2(PO_4)_2$ in 1M K_3PO_4	200	This Work
$Mn_5(H_2O)_4(PO_3OH)_2(PO_4)_2$ in 5M $LiNO_3$	400	This Work
$Mn_5(H_2O)_4(PO_3OH)_2(PO_4)_2$ in 1M Na_2SO_4	375	This Work

It is accepted that a capacitance of 50 μFcm^{-2} can be related only to a pure electric double layer [40,41]. Thus, the large areal capacitance of $Mn_5(H_2O)_4(PO_3OH)_2(PO_4)_2$ indicates that the charge storage process arises from a pseudocapacitive mechanism and a faradaic process, such as ion intercalation into the pocket. In order to understand the charge storage process, the origin of the stored charge must be known. In previous reports, we showed the deconvolution of the cyclic voltammograms of different electrode materials [14,15] to obtain the amount of charge as a function of voltage that arises from the electric double-layer, pseudocapacitive, and faradaic process. The methodology followed to deconvolute the voltammograms is described in the Supporting Information.

In 3M KOH at the scan rate of 5 mVs^{-1}, the charge that arises from a diffusive process (Figure 4a), which in this case is the intercalation of electrolyte ions into the pocket, dominates the charge storage process in all the applied potential. Figure 4b shows the percentage of the charge that arises from the three different processes. It is worth mentioning that even at the high scan rate of 100 mVs^{-1}, around 30 percent of the charge arises from an intercalation process. This is also the case for vanadium phosphates reported in previous work [14]. The charge from the pseudocapacitive process increases with the scan rate (see Figure S5) and can be as high as 40 percent (Figure 4b). The lowest contribution to the charge is from the electric double layer. When 1M KOH was used, the intercalation process was also the main charge storage process across all the applied potential. However, the signature of the plot is different, and the electric double layer is lower than in the previous case. The charge percentage that arises from an intercalation process increases from 65 percent in 3M KOH to 94 percent in 1M KOH at the scan rate of 5 mVs^{-1}. This evidences that the pH and concentration affect the charge storage mechanism. In 1M KOH, both the electric double layer and pseudocapacitive contributions increase with the scan rate (see Figure S6).
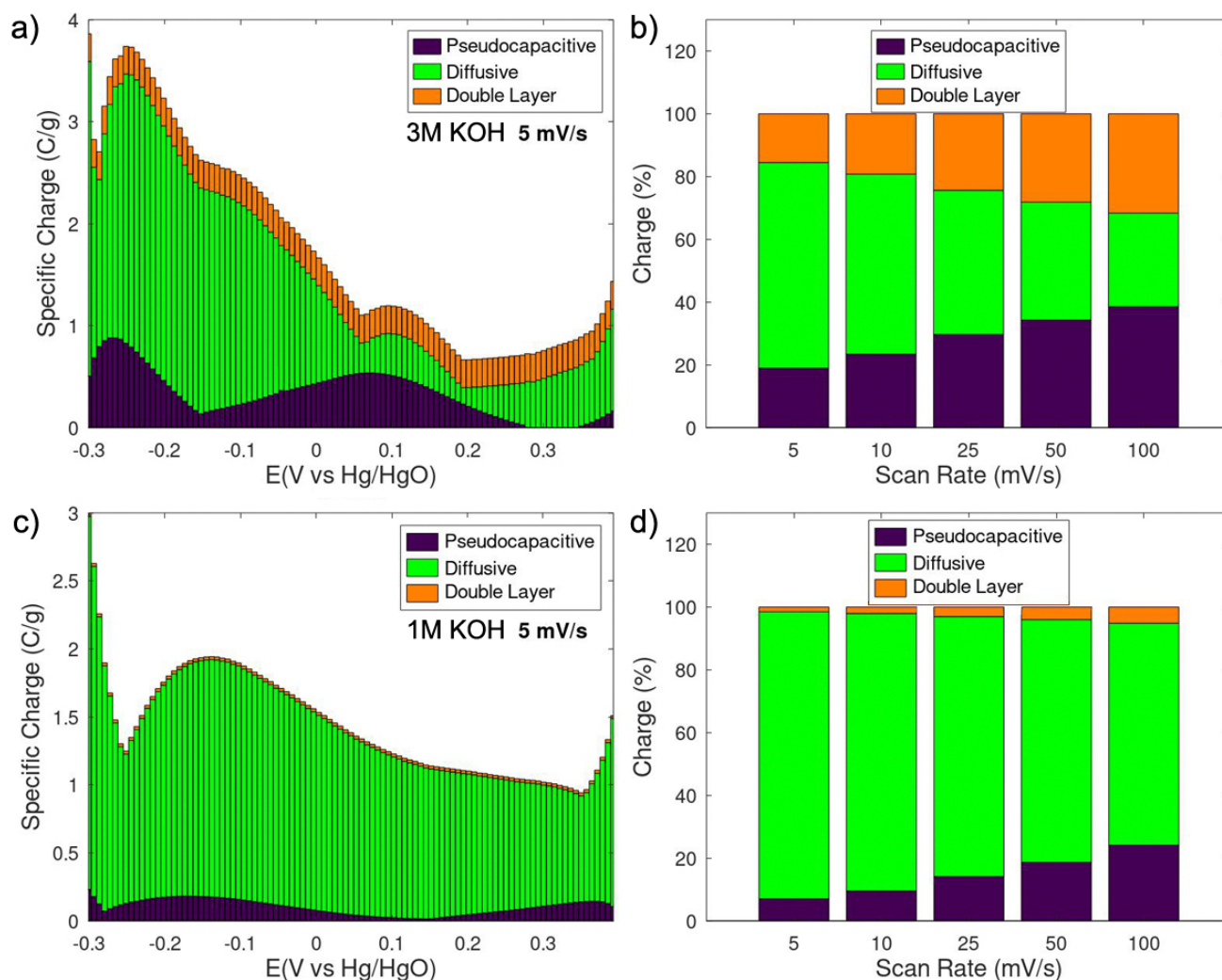
Figure 4. The specific charge of $Mn_5(H_2O)_4(PO_3OH)_2(PO_4)_2$ as a function of applied voltage in alkaline electrolytes (**a**) 3M KOH and (**c**) 1M KOH. Charge percentage as a function of scan rate in (**b**) 3M KOH and (**d**) 1M KOH.

The diffusive process is the main contribution to the charge in 3M NaOH and 3M LiOH in all the applied potential at any scan rate (see Figure 5). However, the amount of charge that arises from the formation of the electric double layer, and a pseudocapacitive process drastically differ in these electrolytes at all the applied scan rates (see Figures S7 and S8). In 3M NaOH, the contribution of pseudocapacitance to the charge storage is more important than the electric double layer at any scan rate. In the case of the 3M LiOH, the contribution of the double layer to the charge storage is as large as 50 percent at high scan rates and more important than pseudocapacitance. Thus, the lower pH of 3M LiOH (12.5) than 3M NaOH (14.0) and 3M KOH (14.6) induces a lower reactivity of the electrolyte for the pseudocapacitive process and the intercalation process, lowering the amount of stored charge.

Interestingly, in 3M TMAOH and 3M K_3PO_4, the deconvoluted cyclic voltammograms show that the main contribution to the stored charge at low scan rates of 5 mVs^{-1} is the intercalation process in all the applied potential (see Figure 6a,c). At higher scan rates (>50 mVs^{-1}), the electric double-layer capacitance and the pseudocapacitive process are the main charge storage processes (see Figure 6b,d).
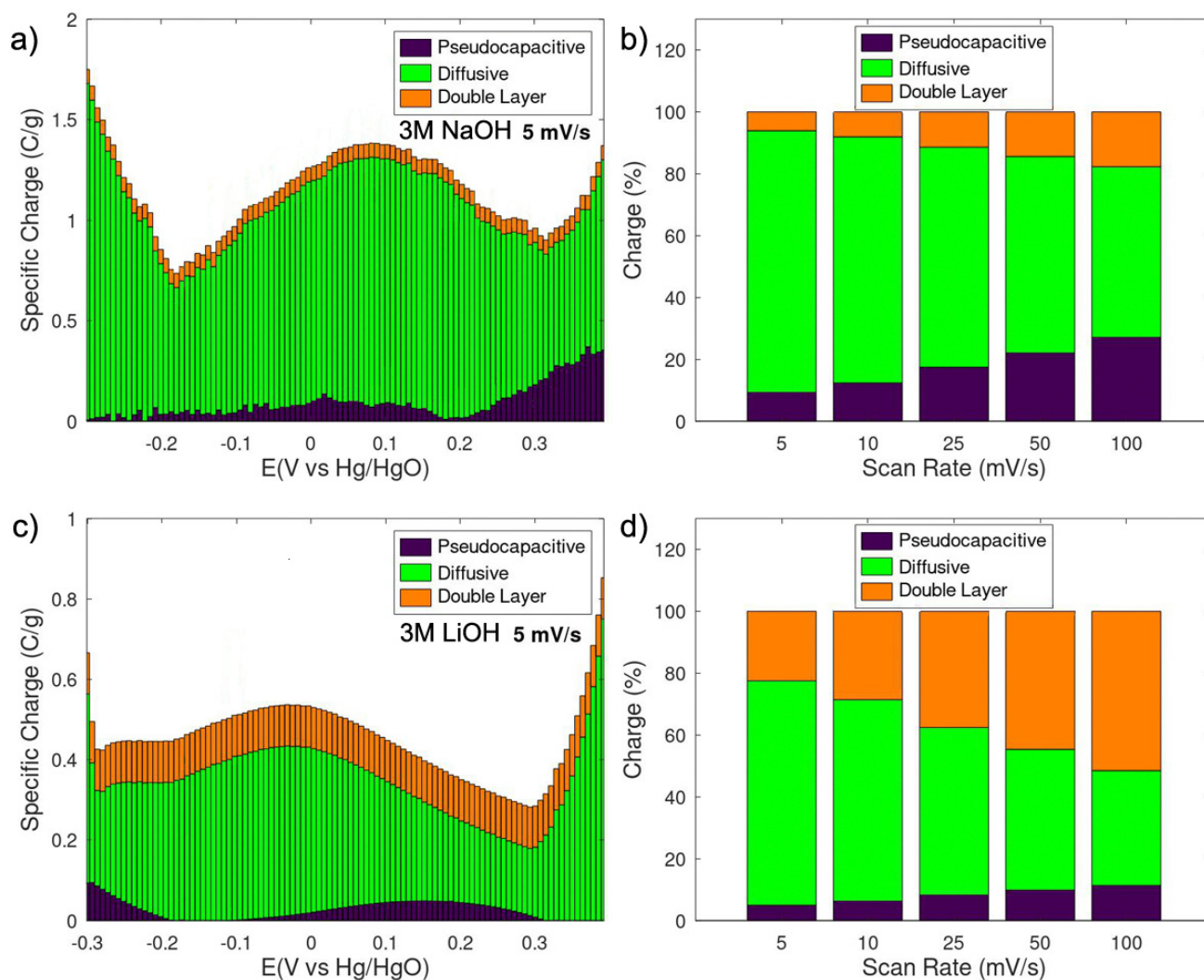
Figure 5. The specific charge of $Mn_5(H_2O)_4(PO_3OH)_2(PO_4)_2$ as a function of applied voltage in alkaline electrolytes (**a**) 3M NaOH and (**c**) 3M LiOH. Charge percentage as a function of scan rate in (**b**) 3M NaOH and (**d**) 3M LiOH.

The specific capacitance is lower than in the previous electrolytes, due to a larger ion size of TMA^+ and PO_4^{3-}, as discussed earlier. However, in 3M TMAOH, the contribution of the electric double layer is more important than in the case of 3M K_3PO_4. This indicates that the TMA^+ induces the formation of the electric double layer (see Figure S9). In 3M K_3PO_4, the pseudocapacitive process is more important to the stored charge (see Figure S10). It is worth mentioning that despite the larger ion size of PO_4^{3-} (2.23, 3.39 Å), a pseudocapacitive and intercalation process takes place. The high pH (14.0) of 3M K_3PO_4 increases the reactivity with the protons inside the pocket (channel size, 6.10 X 3.0 Å). However, the amount of stored charge is lower than in 3M KOH or 3M TMAOH since OH^- is smaller and can increase the ion intercalation through the pocket reacting with more active sites than PO_4^{3-}.

In neutral electrolytes, the amount of stored charge is lower than in 3M KOH and in the same range of 3M K_3PO_4. The deconvoluted charge plots in 5M $LiNO_3$ (see Figure 7a) indicate that the intercalation and pseudocapacitive process takes place across the potential window, and they are around 38 percent of the charge at 5 mVs^{-1}. As the scan rate increases, the pseudocapacitive process becomes dominant up to 58 percent (Figure 7b). The deconvoluted charge vs. applied potential at different scan rates can be observed in Figure S11. The intercalation (diffusion) process becomes less important at high scan rates and the electric double layer and pseudocapacitive process are the main mechanisms of

stored charge. In the case of 1M Na_2SO_4, the intercalation process is observed in all the applied potential window (see Figure 7c) and is as high as 70 percent of the stored charge at 5 mVs^{-1} (see Figure 7d). It is important to notice that the contribution to the electric double layer becomes less important in 1M Na_2SO_4 than in 5M $LiNO_3$ at any scan rate (see Figures 7d and S12). In both neutral electrolytes the pseudocapacitive process becomes dominant at higher scan rates and is as high as 58 percent at the scan rate of 500 mVs^{-1} (see Figure 7c,d). However, the intercalation process is larger in 1M Na_2SO_4, at any scan rate, than in 5M $LiNO_3$. The above suggests that a Na^+ hydrated ion size smaller than that of Li^+ promotes the intercalation. Thus, for an intercalation process into the pocket in neutral pH, the hydrated ion size of cations is more important. In contrast, the contribution of neutral anions to the intercalation process is hindered by their lack of reactivity with the free-O-H acid group in $PO_3(OH)$ tetrahedra. Overall, neutral electrolytes induce a lower amount of stored charge than alkaline electrolytes due to their low reactivity with the O-H acid group located in the pocket. Hence, the stored charge mainly depends on the low specific surface area of $Mn_5(H_2O)_4(PO_3OH)_2(PO_4)_2$ that leads to a lower specific capacitance than in alkaline electrolytes.
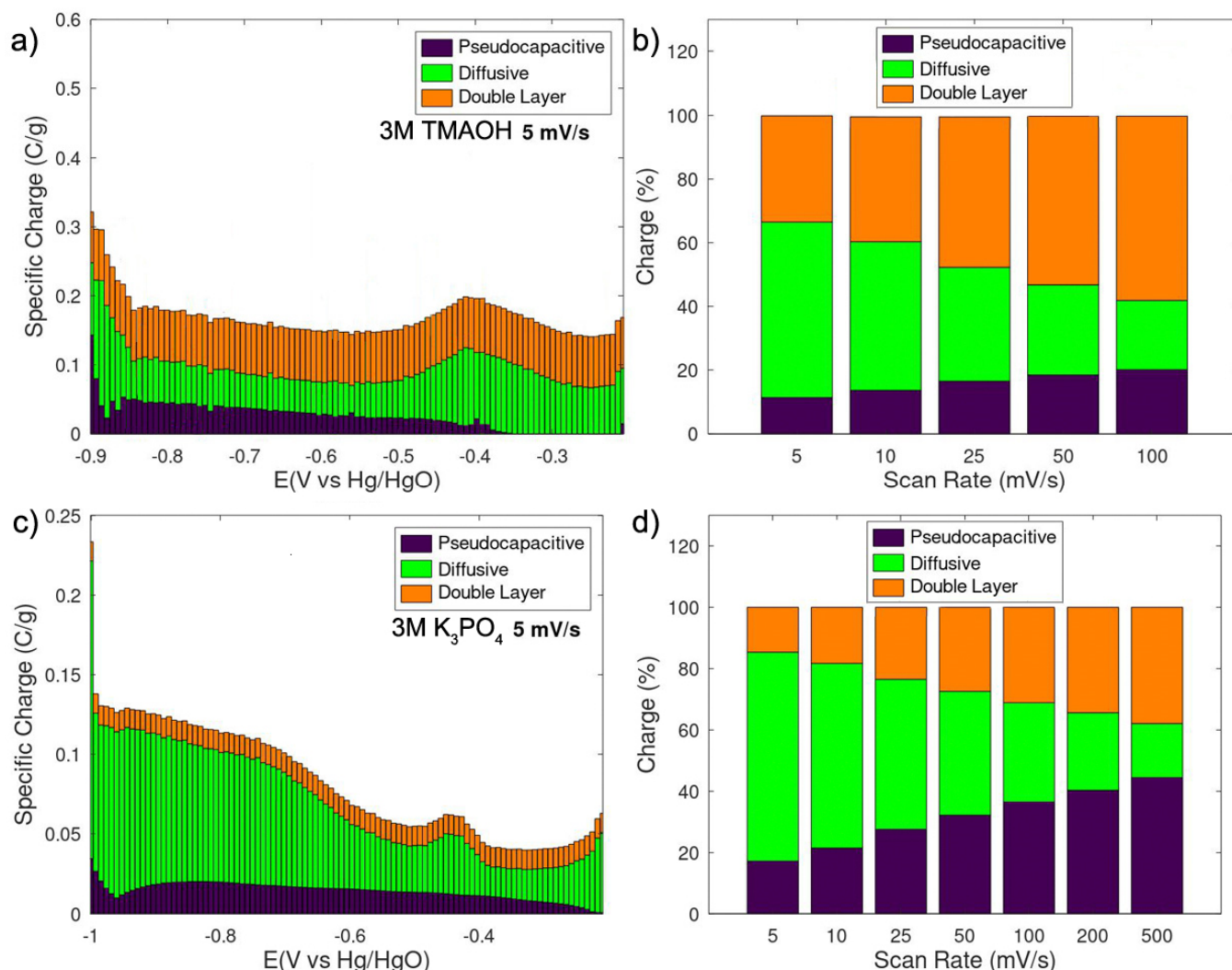

Figure 6. The specific charge of $Mn_5(H_2O)_4(PO_3OH)_2(PO_4)_2$ as a function of applied voltage in alkaline electrolytes (**a**) 3M TMAOH and (**c**) 3M K_3PO_4. Charge percentage as a function of scan rate in (**b**) 3M TMAOH and (**d**) 3M K_3PO_4.
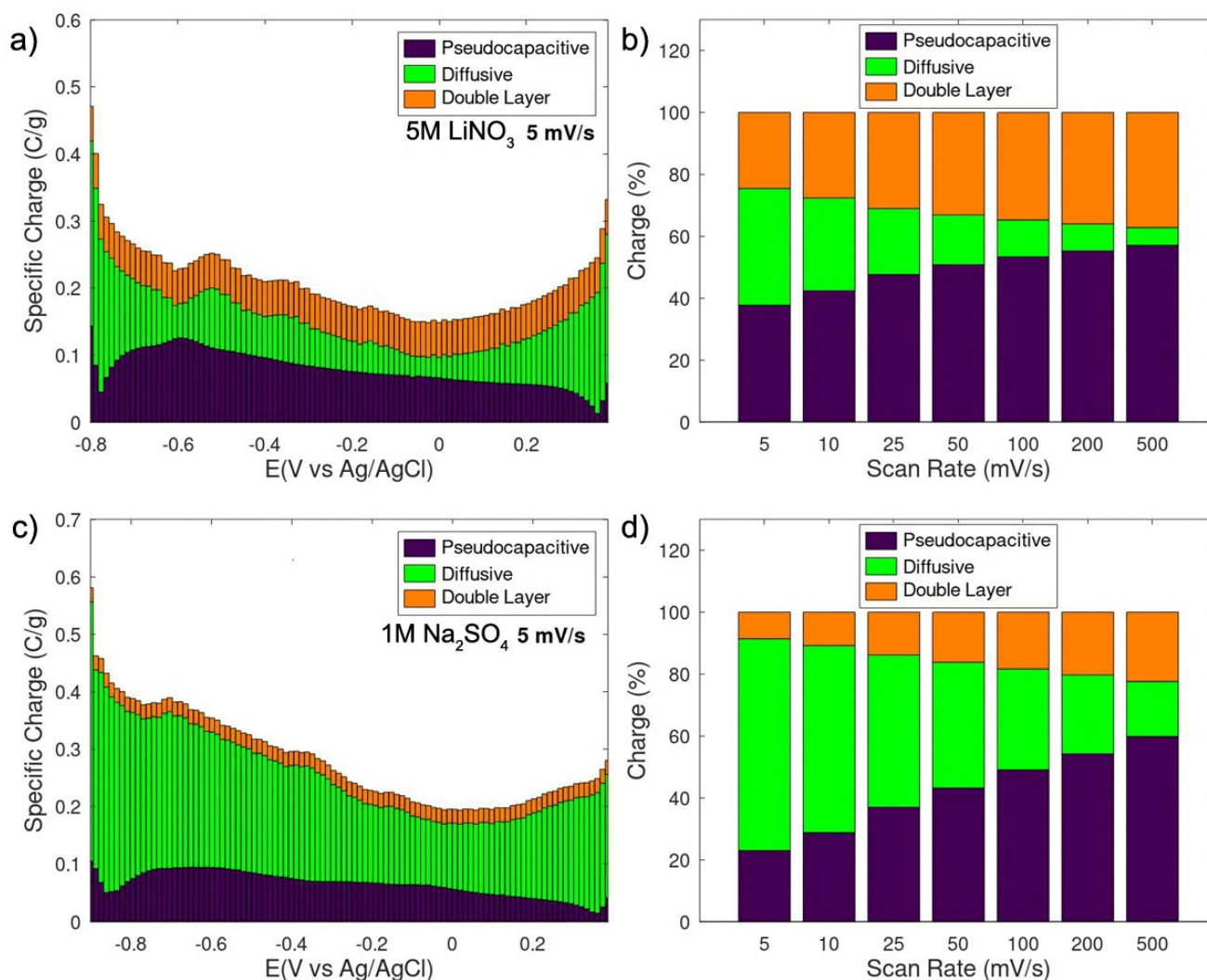
Figure 7. The specific charge of $Mn_5(H_2O)_4(PO_3OH)_2(PO_4)_2$ as a function of applied voltage in neutral electrolytes (**a**) 5M $LiNO_3$ and (**c**) 1M Na_2SO_4. Charge percentage as a function of scan rate in (**b**) 5M $LiNO_3$ and (**d**) 1M Na_2SO_4.

Hence, electrolyte ions can intercalate into the pocket across all of the applied potential. The active thickness represents how deep from the surface the charge storage process takes place via ion intercalation. The methodology used to estimate the active thickness is described in the Supporting Information. In Figure 8a, the active thickness as a function of the applied voltage is estimated in alkaline and neutral electrolytes. The alkaline hydroxides show the highest active thickness. In 3M KOH is as high as 1.6 nm, suggesting a surface–subsurface charge storage process, as expected for electrochemical capacitors.

We propose that the mechanism of ion intercalation involves the concerted formation of O-H bonds via water molecules and the hydrogen atoms of PO_3-OH groups situated in the pocket induced by the acid-base reaction with electrolyte anions (see Figure 8b). As illustrated in Figure 3b, 3M KOH exhibits the highest pH among the alkaline hydroxides, thereby enhancing its reactivity with hydrogen atoms from water molecules. The water molecule closest to the surface reacts with the electrolyte anions (e.g., OH^-), prompting the inner water molecules to donate a proton to compensate the charge of the OH^- group near the surface. This process exemplifies the Grotthuss mechanism of proton conduction [44,45], applied here for the first time in transition metal phosphate for electrochemical capacitors. Notably, this mechanism has also been referenced in the context of high-rate proton batteries and covalent organic frameworks for supercapacitors [46,47]. In the opposite electrode,

cations from the electrolyte are intercalated while the electrode material accumulates a negative charge derived from the current collector.
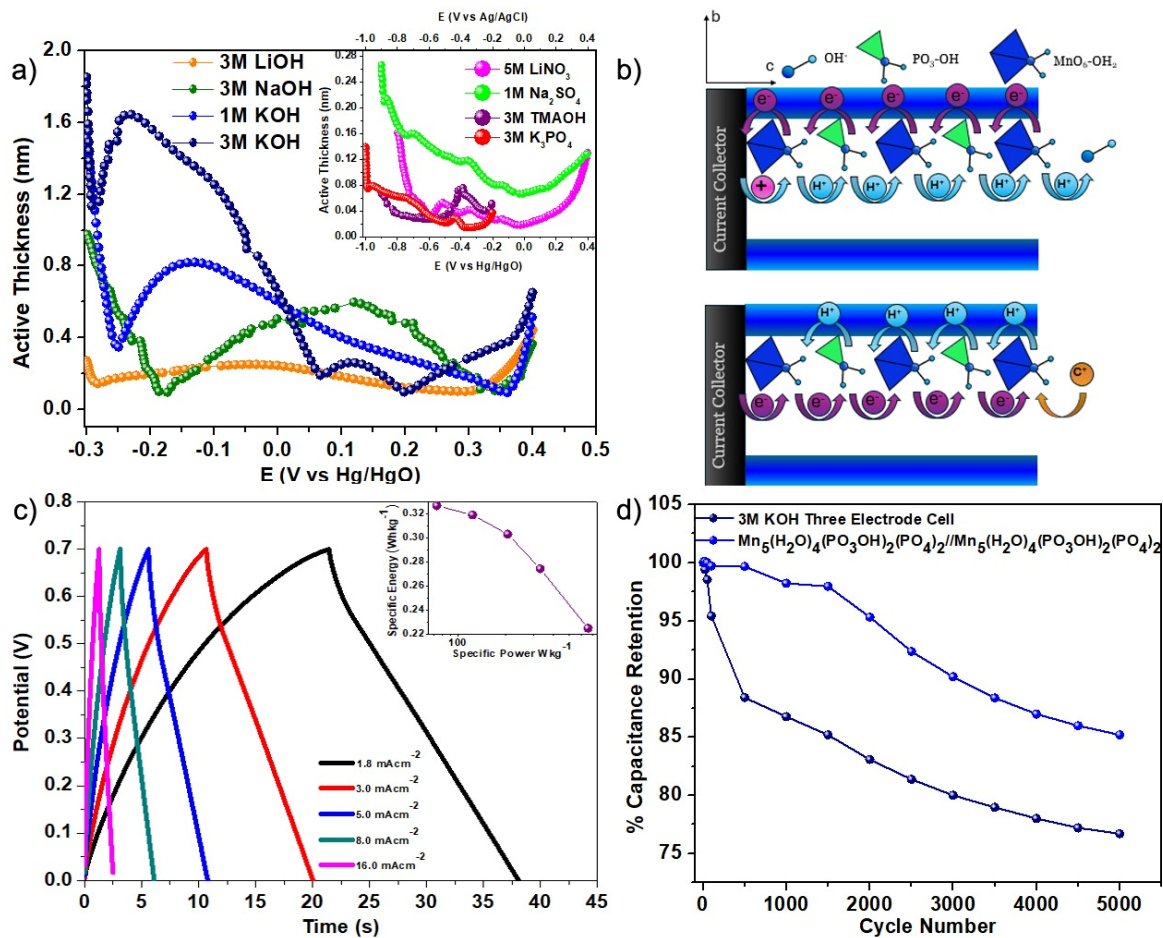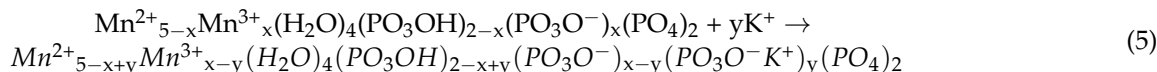

Figure 8. (**a**) Active thickness in different electrolytes. (**b**) Scheme of the proposed mechanism. (**c**) Constant charge–discharge plots of $Mn_5(H_2O)_4(PO_3OH)_2(PO_4)_2$ Swagelok-type device; the inset shows the Ragone plot. (**d**) Percentage of capacitance retention in a three-electrode cell and a two-electrode Swagelok-type cell.

Nevertheless, the open 3D framework structure of $Mn_5(H_2O)_4(PO_3OH)_2(PO_4)_2$ contains more tunnels smaller than the pocket, which cannot allow the entrance of electrolyte ions, but they may contribute to the surface redox process through superficial functional groups such as PO_3-OH and MnO-H. These tunnels probably promote the capacitive response and the surface redox reactions observed at high scan rates in neutral electrolytes, since the electrolyte ions cannot be intercalated into the pocket as discussed earlier. In alkaline electrolytes, these tunnels also promote the charge stored through electric double-layer formation and the pseudocapacitive response through surface redox reactions with the mentioned functional groups.
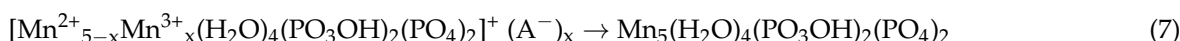
Assigning a specific faradaic process is complex at the moment, but it may concern the redox couple of Mn^{2+}/Mn^{3+} since no manganese phosphate has been reported with Mn^{4+} ions. The following equations show our proposal for the charge storage mechanism in alkaline and neutral electrolytes. For instance, during the anodic scan (Equation (4)) in KOH electrolyte, a proton of the PO_3-OH group reacts with OH^- anions (through the Grotthuss mechanism) with a concerted partial oxidation of Mn^{2+} ions to Mn^{3+}. In the cathodic scan (Equation (5)), K^+ and H^+ ions react with PO_3O^- (an intercalation process) together with a reduction of Mn^{3+} to Mn^{2+}, leading to a reversible process. In neutral electrolytes during the anodic scan (Equation (6)), anions are electroadsorbed with a partial

oxidation of Mn^{2+} to Mn^{3+}. During a cathodic scan (Equation (7)), anions leave the surface, and a reduction of Mn^{3+} ions to Mn^{2+} occurs.

In alkaline electrolytes,

$$Mn^{2+}{}_5(H_2O)_4(PO_3OH)_2(PO_4)_2 + xOH^- \rightarrow Mn^{2+}{}_{5-x}Mn^{3+}{}_x(H_2O)_4(PO_3OH)_{2-x}(PO_3O^-)_x (PO_4)_2 \tag{4}$$

$$Mn^{2+}{}_{5-x}Mn^{3+}{}_x(H_2O)_4(PO_3OH)_{2-x}(PO_3O^-)_x(PO_4)_2 + yK^+ \rightarrow$$
$$Mn^{2+}{}_{5-x+y}Mn^{3+}{}_{x-y}(H_2O)_4(PO_3OH)_{2-x+y}(PO_3O^-)_{x-y}(PO_3O^-K^+)_y(PO_4)_2 \tag{5}$$

In neutral electrolytes, where A is $SO_4{}^{2-}$ or $NO_3{}^-$,

$$Mn^{2+}{}_5(H_2O)_4(PO_3OH)_2(PO_4)_2 + xA^- \rightarrow [Mn^{2+}{}_{5-x}Mn^{3+}{}_x(H_2O)_4(PO_3OH)_2(PO_4)_2]^+(NO_3{}^-)_x \tag{6}$$

$$[Mn^{2+}{}_{5-x}Mn^{3+}{}_x(H_2O)_4(PO_3OH)_2(PO_4)_2]^+ (A^-)_x \rightarrow Mn_5(H_2O)_4(PO_3OH)_2(PO_4)_2 \tag{7}$$

A two-electrode symmetric Swagelok-type cell was assembled, with glass fiber filter as a separator wetted with 0.5 mL of 5M KOH and $Mn_5(H_2O)_4(PO_3OH)_2(PO_4)_2$ as positive and negative electrode material. Figure 8c shows constant charge–discharge cycles with current densities of 1.8, 3.0, 5.0, 8.0, and 16.0 mAcm^{-2} (geometric surface area), with charge time from 1.3 s to 21.5 s. The linear dependence of voltage with time indicates a capacitive like-behavior in agreement with the previous discussion. The cyclic voltammograms shown in Figure S13 illustrate an electrochemical rectangular profile indicating the capacitive-like behavior. The low energy density of the electrode material (see inset Figure 8c) originated from the short-applied voltage in the cell (0.7 V), suggesting the use of $Mn_5(H_2O)_4(PO_3OH)_2(PO_4)_2$ in an asymmetric device. Figure 8d shows the percentage of capacitance retention in two- and three-electrode cells during 5000 cycles of charge and discharge. The capacitance retention is higher in the two-electrode cell with only a 15 percent loss of capacitance (25 percent loss in the three-electrode cell) due to the use of a wetted separator as an electrolyte hindering degradation reactions such as the dissolution of the electrode material.

4. Conclusions

For the first time, $Mn_5(H_2O)_4(PO_3OH)_2(PO_4)_2$ with an open 3D network was prepared and studied as electrode material for electrochemical capacitors. The tunnel structure with a network of hydrogen bonds allows ion intercalation through the Grotthuss proton conduction mechanism. It is also the first time that this mechanism has been applied in electrochemical capacitors based on transition metal phosphates. The alkaline pH of the electrolyte and a small hydrated ion size are the key factors needed to enhance the reactivity with PO_3-OH groups and promote the accumulation of charge in the pocket. Nevertheless, an additional faradaic process is also present, but at the moment, it is difficult to assign a specific reaction. The open 3D network through functional groups also contributes to the pseudocapacitive process with surface reversible redox reactions and electric double-layer capacitance.

In neutral electrolytes, the surface-limited redox reactions observed at high scan rates (above 100 mVs^{-1}) probably also arise from the open 3D network of the $Mn_5(H_2O)_4(PO_3OH)_2(PO_4)_2$ with surface functional groups such as PO_3-OH tetrahedra and MnO_6 units, with bonded water molecules that react with electrolyte ions enabling a fast electrochemical charge storage process. Hence, increasing the specific surface area of these materials would allow a larger amount of stored charge.

The electrochemical behavior at high scan rates in neutral and alkaline electrolytes with an evident faradaic process indicates the potential application of $Mn_5(H_2O)_4(PO_3OH)_2(PO_4)_2$ for fast electrochemical energy storage devices. Additionally, the two-electrode cell test shows the potential application of $Mn_5(H_2O)_4(PO_3OH)_2(PO_4)_2$ as electrode material in a complete device due to its high capacitance retention after 5000 charge–discharge cycles.

References

1. Fu, W.; Turcheniuk, K.; Naumov, O.; Mysyk, R.; Wang, F.; Liu, M.; Kim, D.; Ren, X.; Magasinski, A.; Yu, M.; et al. Materials and technologies for multifunctional, flexible or integrated supercapacitors and batteries. *Mater. Today* **2021**, *48*, 176–197. [CrossRef]
2. Choi, C.; Ashby, D.S.; Butts, D.M.; DeBlock, R.H.; Wei, Q.; Lau, J.; Dunn, B. Achieving high energy density and high power density with pseudocapacitive materials. *Nat. Rev. Mater.* **2020**, *5*, 5–19. [CrossRef]
3. Simon, P.; Gogotsi, Y.; Dunn, B. Where Do Batteries End and Supercapacitors Begin? *Science* **2014**, *343*, 1210–1211. [CrossRef] [PubMed]
4. Zhao, J.; Burke, A.F. Review on supercapacitors: Technologies and performance evaluation. *J. Energy Chem.* **2021**, *59*, 276–291. [CrossRef]
5. Liang, R.; Du, Y.; Xiao, P.; Cheng, J.; Yuan, S.; Chen, Y.; Yuan, J.; Chen, J. Transition Metal Oxide Electrode Materials for Supercapacitors: A Review of Recent Developments. *Nanomaterials* **2021**, *11*, 1248. [CrossRef] [PubMed]
6. Cao, Z.; Momen, R.; Tao, S.; Xiong, D.; Song, Z.; Xiao, X.; Deng, W.; Hou, H.; Yasar, S.; Altin, S.; et al. Metal–Organic Framework Materials for Electrochemical Supercapacitors. *Nano-Micro Lett.* **2022**, *14*, 181. [CrossRef] [PubMed]
7. Lucio-Porto, R.; Bouhtiyya, S.; Pierson, J.; Morel, A.; Capon, F.; Boulet, P.; Brousse, T. VN thin films as electrode materials for electrochemical capacitors. *Electrochim. Acta* **2014**, *141*, 203–211. [CrossRef]
8. Brian Evans Conway. Electrochemical Supercapacitors. In *Scientific Fundamentals and Technological Applications*, 1st ed.; Kluwer Academic/Plenum Publisher: New York, NY, USA, 1999.
9. Boyd, S.; Ganeshan, K.; Tsai, W.-Y.; Wu, T.; Saeed, S.; Jiang, D.-E.; Balke, N.; van Duin, A.C.T.; Augustyn, V. Effects of interlayer confinement and hydration on capacitive charge storage in birnessite. *Nat. Mater.* **2021**, *20*, 1689–1694. [CrossRef]
10. Panigrahi, K.; Howli, P.; Chattopadhyay, K.K. 3D network of V2O5 for flexible symmetric supercapacitor. *Electrochim. Acta* **2020**, *337*, 135701. [CrossRef]
11. Majumdar, D.; Mandal, M.; Bhattacharya, S.K. V_2O_5 and its Carbon-Based Nanocomposites for Supercapacitor Applications. *ChemElectroChem* **2018**, *6*, 1623–1648. [CrossRef]
12. Mitchell, J.B.; Lo, W.C.; Genc, A.; LeBeau, J.; Augustyn, V. Transition from Battery to Pseudocapacitor Behavior via Structural Water in Tungsten Oxide. *Chem. Mater.* **2017**, *29*, 3928–3937. [CrossRef]
13. Porto, R.L.; Cortez, I.E.M.; Brousse, T.; Martínez, J.A.A.; Pavón, L.A.L. MnPO$_4 \cdot$H$_2$O as Electrode Material for Electrochemical Capacitors. *J. Electrochem. Soc.* **2018**, *165*, A2349–A2356. [CrossRef]
14. Martínez, J.A.Z.; Náñez, S.E.G.; Le Calvez, E.; Porto, R.L.; Cortez, I.E.M.; Brousse, T.; Pavón, L.A.L. Layered Vanadium Phosphates as Electrodes for Electrochemical Capacitors Part I: The case of VOPO$_4 \cdot$2H$_2$O. *J. Electrochem. Soc.* **2021**, *168*, 070531. [CrossRef]
15. Martínez, J.A.Z.; Náñez, S.E.G.; Le Calvez, E.; Porto, R.L.; Cortez, I.E.M.; Brousse, T.; Pavón, L.A.L. Layered Vanadium Phosphates as Electrodes for Electrochemical Capacitors Part II: The case of VOPO$_4 \cdot$CTAB and K$_{0.5}$VOPO$_4 \cdot$1.5H$_2$O. *J. Electrochem. Soc.* **2021**, *168*, 090520. [CrossRef]
16. Bao, X.; Zhang, W.-B.; Zhang, L.; Guo, Y.-W.; Zhou, X.; Zhang, X.-L.; Han, X.-W.; Long, J. Alkali cation intercalation manganese phosphate hydrate boosting electrochemical kinetics for pseudocapacitive energy storage. *J. Mater.* **2022**, *8*, 833–842. [CrossRef]
17. Pan, M.-Y.; Lu, S.-T.; Li, Y.-Y.; Fan, Y. Synthetic hureaulite as anode material for lithium-ion batteries. *J. Appl. Electrochem.* **2023**, *53*, 1015–1022. [CrossRef]
18. Moore, P.B.; Araki, T. Hureaulite, Mn$_5^{2+}$(H$_2$O)$_4$[PO$_3$(OH)]$_2$[PO$_4$]$_2$: Its atomic arrangement. *Am. Mineral.* **1973**, *58*, 302–307. Available online: http://www.minsocam.org/ammin/AM58/AM58_302.pdf (accessed on 7 April 2024).
19. Menchetti, S.; Sabelli, C. The crystal structure of hureaulite, Mn$_5$(HOPO$_3$)$_2$(PO$_4$)$_2$(H$_2$O)$_4$. *Acta Crystallogr. Sect. B Struct. Crystallogr. Cryst. Chem.* **1973**, *29*, 2541–2548. [CrossRef]

20. De Amorim, H.S.; Amaral, M.R.D.; Moreira, L.F.; Mattievich, E. Structure refinement of synthetic hureaulite: $Mn_5(H_2O)_4[PO_3(OH)]_2[PO_4]_2$. *J. Mater. Sci. Lett.* **1996**, *15*, 1895–1897. [CrossRef]

21. Gatta, G.D.; Redhammer, G.J.; Vignola, P.; Meven, M.; McIntyre, G.J. Single-crystal neutron diffraction and Mössbauer spectroscopic study of hureaulite, $(MnFe)_5(PO_4)_2(HPO_4)_2(H_2O)_4$. *Eur. J. Mineral.* **2016**, *28*, 93–103. [CrossRef]

22. Hartl, A.; Park, S.-H.; Hoelzel, M.; Paul, N.; Gilles, R. Proton conductivity in a hureaulite-type compound, $Mn_5[(PO_4)_2(PO_3(OH))_2](HOH)_4$. *J. Solid State Chem.* **2019**, *277*, 290–302. [CrossRef]

23. Qiu, G.; Gao, Z.; Yin, H.; Feng, X.; Tan, W.; Liu, F. Synthesis of $MnPO_4 \cdot H_2O$ by refluxing process at atmospheric pressure. *Solid State Sci.* **2010**, *12*, 808–813. [CrossRef]

24. Yin, H.; Liu, F.; Chen, X.; Feng, X.; Tan, W.; Qiu, G. Synthesis of hureaulite by a reflux process at ambient temperature and pressure. *Microporous Mesoporous Mater.* **2012**, *153*, 115–123. [CrossRef]

25. Sronsri, C.; U-Yen, K.; Sittipol, W. Application of synthetic hureaulite as a new precursor for the synthesis of lithiophilite nanoparticles. *Solid State Sci.* **2020**, *110*, 106469. [CrossRef]

26. Frost, R.L.; Xi, Y.; Scholz, R.; López, A.; Belotti, F.M. Vibrational spectroscopic characterization of the phosphate mineral hureaulite—$(Mn, Fe)_5(PO_4)_2(HPO_4)_2 \cdot 4(H_2O)$. *Vib. Spectrosc.* **2013**, *66*, 69–75. [CrossRef]

27. Aranda, M.A.G.; Bruque, S. Characterization of manganese(III) orthophosphate hydrate. *Inorg. Chem.* **1990**, *29*, 1334–1337. [CrossRef]

28. Boonchom, B.; Youngme, S.; Maensiri, S.; Danvirutai, C. Nanocrystalline serrabrancaite ($MnPO_4 \cdot H_2O$) prepared by a simple precipitation route at low temperature. *J. Alloys Compd.* **2008**, *454*, 78–82. [CrossRef]

29. Šoptrajanov, B.; Stefov, V.; Kuzmanovski, I.; Jovanovski, G. Fourier transform infrared and Raman spectra of manganese hydrogenphosphate trihydrate. *J. Mol. Struct.* **1999**, *482–483*, 103–107. [CrossRef]

30. Yang, C.; Dong, L.; Chen, Z.; Lu, H. High-Performance All-Solid-State Supercapacitor Based on the Assembly of Graphene and Manganese(II) Phosphate Nanosheets. *J. Phys. Chem. C* **2014**, *118*, 18884–18891. [CrossRef]

31. Ma, X.-J.; Zhang, W.-B.; Kong, L.-B.; Luo, Y.-C.; Kang, L. Electrochemical performance in alkaline and neutral electrolytes of a manganese phosphate material possessing a broad potential window. *RSC Adv.* **2016**, *6*, 40077–40085. [CrossRef]

32. Mirghni, A.A.; Madito, M.J.; Masikhwa, T.M.; Oyedotun, K.O.; Bello, A.; Manyala, N. Hydrothermal synthesis of manganese phosphate/graphene foam composite for electrochemical supercapacitor applications. *J. Colloid Interface Sci.* **2017**, *494*, 325–337. [CrossRef] [PubMed]

33. Ji, C.-C.; Xu, M.-W.; Bao, S.-J.; Cai, C.-J.; Wang, R.-Y.; Jia, D.-Z. Effect of alkaline and alkaline–earth cations on the supercapacitor performance of $MnO2$ with various crystallographic structures. *J. Solid State Electrochem.* **2013**, *17*, 1357–1368. [CrossRef]

34. Choi, D.; Blomgren, G.E.; Kumta, P.N. Fast and Reversible Surface Redox Reaction in Nanocrystalline Vanadium Nitride Supercapacitors. *Adv. Mater.* **2006**, *18*, 1178–1182. [CrossRef]

35. Zhou, M.; Vassallo, A.; Wu, J. Data-Driven Approach to Understanding the *In-Operando* Performance of Heteroatom-Doped Carbon Electrodes. *ACS Appl. Energy Mater.* **2020**, *3*, 5993–6000. [CrossRef]

36. Zhong, C.; Deng, Y.; Hu, W.; Qiao, J.; Zhang, L.; Zhang, J. A review of electrolyte materials and compositions for electrochemical supercapacitors. *Chem. Soc. Rev.* **2015**, *44*, 7484–7539. [CrossRef] [PubMed]

37. Lucio-Porto, R.; Gómez, I. Synthesis of Manganese Oxide Nanocompounds for Electrodes in Electrochemical Capacitors. *Synth. React. Inorg. Met. Nano-Metal Chem.* **2012**, *42*, 833–838. [CrossRef]

38. Porto, R.L.; Frappier, R.; Ducros, J.; Aucher, C.; Mosqueda, H.; Chenu, S.; Chavillon, B.; Tessier, F.; Cheviré, F.; Brousse, T. Titanium and vanadium oxynitride powders as pseudo-capacitive materials for electrochemical capacitors. *Electrochim. Acta* **2012**, *82*, 257–262. [CrossRef]

39. Zhu, Y.; Qian, Y.; Ju, Z.; Ji, Y.; Yan, Y.; Liu, Y.; Yu, G. Understanding Charge Storage in Hydrated Layered Solids $MOPO_4$ (M = V, Nb) with Tunable Interlayer Chemistry. *ACS Nano* **2020**, *14*, 13824–13833. [CrossRef]

40. Trasatti, S. Effect of the nature of the metal on the dielectric properties of polar liquids at the interface with electrodes. A phenomenological approach. *J. Electroanal. Chem. Interfacial Electrochem.* **1981**, *123*, 121–139. [CrossRef]

41. Zhang, Y.; Feng, H.; Wu, X.; Wang, L.; Zhang, A.; Xia, T.; Dong, H.; Li, X.; Zhang, L. Progress of electrochemical capacitor electrode materials: A review. *Int. J. Hydrogen Energy* **2009**, *34*, 4889–4899. [CrossRef]

42. Jeong, M.-G.; Zhuo, K.; Cherevko, S.; Kim, W.-J.; Chung, C.-H. Facile preparation of three-dimensional porous hydrous ruthenium oxide electrode for supercapacitors. *J. Power Sources* **2013**, *244*, 806–811. [CrossRef]

43. Brousse, T.; Toupin, M.; Dugas, R.; Athouel, L.; Crosnier, O.; Bélanger, D. Crystalline MnO_2 as Possible Alternatives to Amorphous Compounds in Electrochemical Supercapacitors. *J. Electrochem. Soc.* **2006**, *153*, A2171. [CrossRef]

44. De Grotthuss, C.J.T. Mémoire sur la décomposition de l'eau: Et des corps qu'elle tient en dissolution à l'aide de l'électricité galvanique. *Ann. Chim.* **1806**, *58*, 54–75.

45. Marx, D. Proton Transfer 200 Years after von Grotthuss: Insights from Ab Initio Simulations. *Chemphyschem* **2006**, *7*, 1848–1870. [CrossRef] [PubMed]

46. Zhao, Q.; Song, A.; Zhao, W.; Qin, R.; Ding, S.; Chen, X.; Song, Y.; Yang, L.; Lin, H.; Li, S.; et al. Boosting the Energy Density of Aqueous Batteries via Facile Grotthuss Proton Transport. *Angew. Chem.* **2020**, *133*, 4215–4220. [CrossRef]

47. Yang, Y.; Zhang, P.; Hao, L.; Cheng, P.; Chen, Y.; Zhang, Z. Grotthuss Proton-Conductive Covalent Organic Frameworks for Efficient Proton Pseudocapacitors. *Angew. Chem. Int. Ed.* **2021**, *60*, 21838–21845. [CrossRef] [PubMed]

48.   Ardizzone, S.; Fregonara, G.; Trasatti, S. Inner and Outer active surface of RuO$_2$ electrodes. *Electrochem. Acta* **1990**, *35*, 263. [CrossRef]

49.   Brezesinski, T.; Wang, J.; Polleux, J.; Dunn, B.; Tolbert, S.H. Templated Nanocrystal-Based Porous TiO$_2$ Films for Next-Generation Electrochemical Capacitors. *J. Am. Chem. Soc.* **2009**, *131*, 1802–1809. [CrossRef]